

Quantifying synergy and redundancy in multiplex networks

Andrea I Luppi,^{1,2,*} Eckehard Olbrich,³ Conor Finn,³ Laura E. Suárez,²

Fernando E. Rosas,^{4,5,6,7} Pedro A.M. Mediano,⁸ Jürgen Jost^{3,9,10}

¹*Division of Anaesthesia and Department of Clinical Neurosciences, University of Cambridge, Cambridge, UK*

²*Montreal Neurological Institute, McGill University, Montréal, Canada*

³*Max Planck Institute for Mathematics in the Sciences, Leipzig, Germany*

⁴*Department of Informatics, University of Sussex, Brighton, UK*

⁵*Centre for complexity science, Imperial College London, London, UK*

⁶*Centre for psychedelic research, Department of Brain Sciences, Imperial College London, London, UK*

⁷*Centre for Eudaimonia and human flourishing, University of Oxford, Oxford, UK*

⁸*Department of Computing, Imperial College London, London, UK*

⁹*ScaDS.AI, Leipzig University, Germany*

¹⁰*Santa Fe Institute, Santa Fe, USA*

Abstract

Understanding how different networks relate to each other is key for obtaining a greater insight into complex systems. Here, we introduce an intuitive yet powerful framework to characterise the relationship between two networks, comprising the same nodes. We showcase our framework by decomposing the shortest paths between nodes as being contributed uniquely by one or the other source network, or redundantly by either, or synergistically by the two together. Our approach takes into account the networks' full topology, but it also provides insights at multiple levels of resolution: from global statistics, to individual paths of different length. We show that this approach is widely applicable, from brains to the London transport system. In humans and across 123 other species, we demonstrate that reliance on unique contributions by long-range white matter fibers is a conserved feature of mammalian structural connectomes. Across species, we also find that efficient communication relies on significantly greater synergy between long-range and short-range fibers than expected by chance, and significantly less redundancy. Our framework may find applications to help decide how to trade-off different desiderata when designing network systems, or to evaluate their relative presence in existing systems, whether biological or artificial.

Introduction

Networks provide an intuitive representation of systems with interacting components, enabling the use of rigorous mathematical tools to study complex systems across domains of science. A useful way for leveraging network representations involves assessing the (dis)similarity between the topologies of two networks built upon the same underlying nodes. For example, one may want to compare the train and flight transportation networks linking a given set of cities, compare different modes of social interaction between the same group of people, or contrast different types of connections bridging different brain areas. Approaches to this question usually are based on comparing different network topologies in terms of their 'distance'; various scalar metrics have been introduced for this purpose [1–4]. However, these approaches tend to characterise the divergence between networks in terms of a single number, thus yielding a one-dimensional description of a potentially rich discrepancy.

Here we introduce a new framework that characterises the similarity between networks using a multidimensional approach, which brings to light different ways in which networks can be (dis)similar and — most importantly —

complementary to each other. Our approach draws inspiration from the literature on Partial Information Decomposition (PID), which develops the principle that information is not a monolithic entity but can be disentangled into qualitatively different types, including redundancy (information that can be independently retrieved in more than one source), unique (information that can be only retrieved from a specific source), and synergy (information that cannot be retrieved from a single source, but only by taking into account multiple sources at once). Inspired by the PID framework, in this paper we introduce the *partial network decomposition* (PND): a formalism that disentangles the relationship between networks in terms of different 'similarity modes'. We showcase how PND allows to gain new insights into artificial and biological networks by analysing two scenarios: London's public transportation systems, and the topologies of short- vs long-range connections in the brains of humans and over 100 other mammalian species.

* Correspondence: al857@cam.ac.uk

Results

Conceptualising synergy and redundancy of networks

Our central question is whether two networks built over the same nodes can be considered synergistic, or redundant. Intuitively, two networks can be said to be redundant if their joint structure is equivalent to the structure of each. Conversely, one could say that they are synergistic if, when considered together, the two networks complement each other in some sense. Let’s illustrate this principle in the case of transport networks: when considering the topologies of e.g. bus and train networks, synergy occurs if the best way — in terms of cost, or time — to move between stations involves using both modalities. In contrast, the two networks are redundant if each provides alternative routes of equal efficiency, and their combination does not provide additional gains.

To capitalise on this intuition, let us consider two undirected, unweighted (binary), connected networks (with no isolated nodes) predicated on the same set of nodes, denoted by A and B . One can identify synergy between networks A and B whenever the most efficient (shortest) path between two nodes x and y involves traversing a combination of edges from A and B . Practically, this means that the most efficient path between x and y is found on the joint network, constructed by placing an edge between each pair of nodes that are directly connected in either network A or network B , such that the joint is also an unweighted and undirected network. One can then operationalise efficient paths between nodes x and y over networks A and B as being redundant if they are of equal length — such that a traveller would be indifferent between traversing via network A or B ¹. Finally, if the most efficient path between nodes x and y is shorter in network A (respectively, B) than in network B (resp., A), then it is natural to label it as “unique” to network A (resp., B). Thus, if the most efficient path between nodes x and y is of length l_A when only using edges from network A , of length l_B when only using edges belonging to network B , and of length $l_{A \cup B}$ when using edges from A and B , then the classification of the link between x and y can be done according to the following procedure:

- Synergistic if $\min\{l_A, l_B\} > l_{A \cup B}$.
- Unique if $\min\{l_A, l_B\} = l_{A \cup B}$ and also $\max\{l_A, l_B\} > l_{A \cup B}$.
- Redundant if $\max\{l_A, l_B\} = l_{A \cup B}$.

It is direct to verify that this procedure identifies the most efficient (shortest) path between a pair of nodes x

and y as being synergistic, redundant, or unique to either network A or B , with no other outcome being possible.

Following this rationale, we can obtain a global quantification of the prevalence of synergistic, redundant, and unique paths across the two networks in terms of the proportion of all shortest paths that they respectively account for, which answers the following question: how many of the possible maximally efficient paths between nodes would an agent know if they knew a map of network A , or a map of network B , or both maps?

Finally, in addition to this global-level insight, our approach also allows us to obtain further refined insight by focusing on the relevance of different scales (i.e., paths of different length). In effect, it is possible that the interactions between the two networks may be different for paths of different length — e.g. short paths may be more redundant while longer ones are more synergistic. Our method provides a straightforward way to obtain such insight: since it provides a decomposition of the efficiency between each pair of nodes, one can simply group the network’s shortest paths in terms of their length l , and check the proportion of them that are synergistic/redundant/unique.²

Partial network decomposition in random network models

To build some initial intuitions on how different networks may contribute to the most efficient paths of a combined network, we constructed pairs of Erdős-Rényi networks of different densities (ranging from 1% to 100%), and evaluated the synergistic, redundant, and unique contributions between them. Results show that shorter paths become less synergistic and more redundant as the density of links grows (see Fig. 1A). In effect, the majority of maximally efficient paths on the joint network are synergistic when the networks are both sparse (i.e. both with densities of 5% or less). Synergy is also present up to approximately 15% density, thereafter dropping off rapidly. Unique contributions from one network tend to dominate, when the other network is below approximately 15% density, thereafter also levelling off rapidly. Thus, when the two networks’ densities are imbalanced, unique contributions from the denser one tend to predominate. Conversely, when the two networks have similar density (and both above 15% density), then the majority of the maximally efficient paths are redundant, with redundancy increasing gradually with both networks’ density (Fig. 1B).

¹ Note that this differs from having multiple paths between x and y within network A or network B [5]: what we care about is that x and y be reachable in the same number of steps within network A and within network B .

² Note that length-1 paths (which correspond to direct edges) can only be, by definition, either redundant or unique.

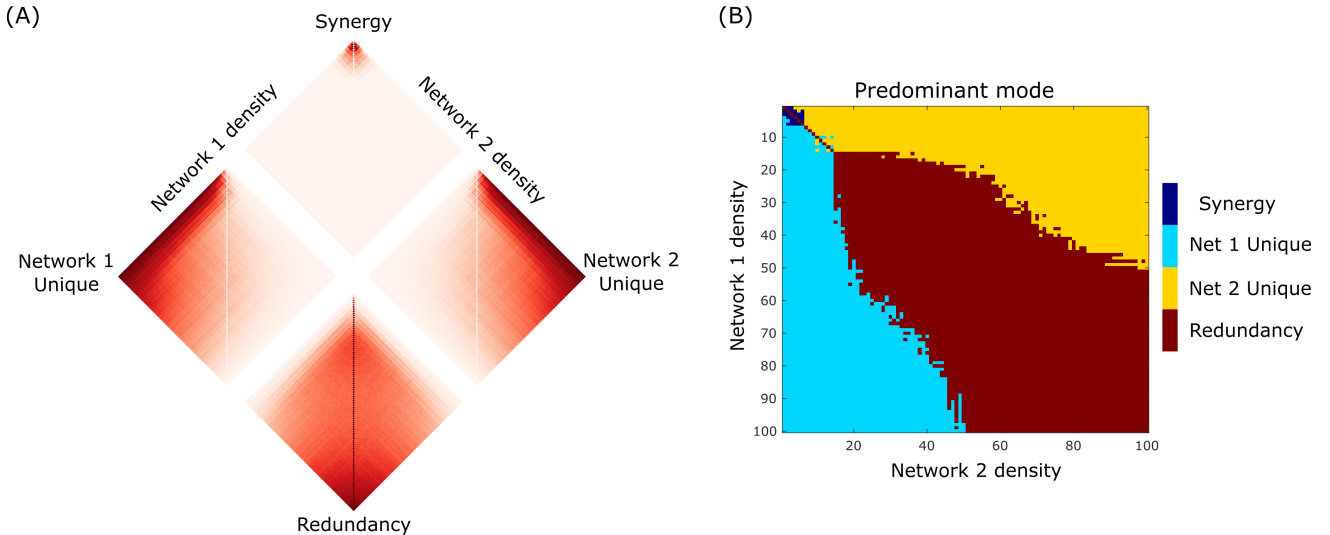


Figure 1. **Contributions to shortest paths as a function of network density.** (A) Each contribution as a function of both networks' density. (B) Component accounting for the majority of shortest paths, as a function of both networks' density.

London transport network

We then analysed real data from a context that may be familiar to everyday life — transportation networks. We investigated the topologies of two means of transportation in London: underground (i.e. subway) and overground (including different types of local trains) (Fig. 2A). We used PND to gain insight on how these two types of transportation serve the needs of Londoners to move within the city.

Our analyses reveal that there is extremely low redundancy between the topologies of underground and overground. Other similarity modes, however, exhibit a strong dependence on the length of the path. For example, short paths show an approximately 70% unique contribution from underground and nearly 30% contribution from overground. Synergy rises rapidly with path length, accounting for over 60% of all paths at its peak, and over 50% of paths of most lengths. This changes rapidly at the very longest paths, where again Underground unique paths predominate, eventually reaching 100% contribution (Fig. 2B). Overall, these findings speak about the efficiency of the design of these networks, which serve the city with almost no redundancy and substantial synergy.

To evaluate the significance of these findings, we compared the obtained results against the decomposition arising from a null distribution involving randomly rewiring each of the two networks, while preserving the degree sequence to account for the potential confounding effects of this low-level network property (Fig. 2C). We found that the London transport network relies on unique contributions from the underground network significantly more than would be expected by chance ($p = 0.007$). Intriguingly, although redundancy is by far the least prevalent term in the decomposition, its value is nevertheless

less significantly greater ($p < 0.001$) than what would be expected based on two random networks of equal density and degree sequence (Fig. 2C). The other two contributions (overground and synergy) did not significantly differ from their degree-preserving null counterparts. However, when null distributions were obtained using purely random networks (with same density as the original ones) instead of degree-preserving random networks, the unique contribution of the overground network was also significantly greater than expected from chance ($p < 0.001$), whereas the contribution of synergy was significantly lower than expected from chance ($p = 0.002$). Thus, we see that the degree sequence plays a role in determining the decomposition.

Connectivity networks in the human brain

The next step in our analysis was to investigate the relationship between the networks of long-range and short-range white matter fibers that link different regions within the human brain (note that we use short-range and long-range to refer to the physical length of fibers in millimetres, determined by the Euclidean distance between the two regions they connect). White matter fibers provide the anatomical scaffold over which communication unfolds in the brain; understanding how their networked organisation supports brain function is a major topic of research in neuroscience [6].

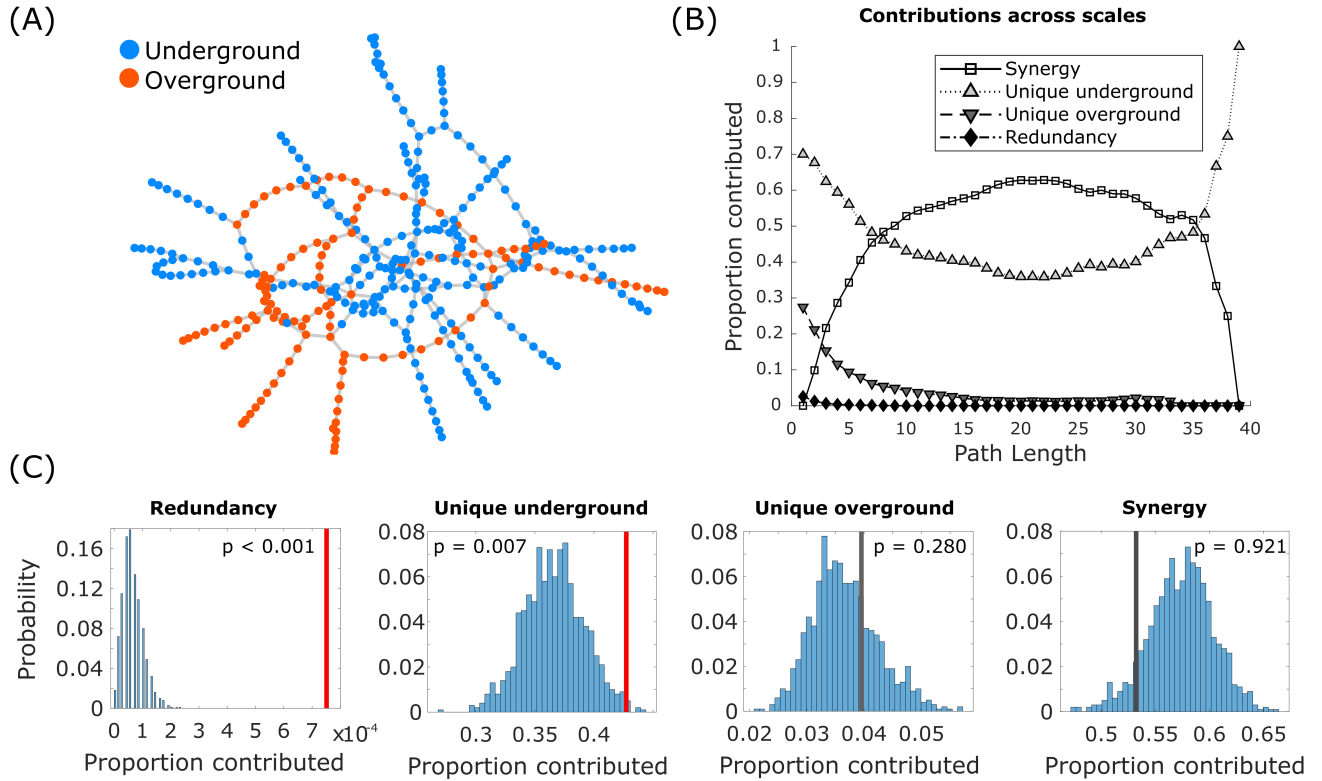


Figure 2. **London transport networks.** (A) The underground network (blue) and the overground network (orange). (B) The relative proportion of shortest paths accounted for by redundant, unique, and synergistic contributions, as a function of path length. (C) Empirical results (vertical lines) against a null distribution obtained from degree-preserving randomisation of the two networks. Red line indicates statistical significance.

We used the PND framework to investigate the network topology of long-range and short-range white matter tracts reconstructed from in-vivo diffusion MRI tractography in 100 healthy human adults (see Methods). For each subject, we defined one network as comprising the 50% physically longest fibers in that subject’s brain; and a second network as comprising the 50% physically shortest white matter fibers. Thus, the two networks have equal density. As a first (subject-level) analysis, we decomposed the similarity of the long- and short-range connections observed in each subject.

Results revealed that, on average across individuals, nearly 50% of the maximally efficient paths in the overall connectome (combining long-range and short-range fibers) are accounted for by long-range white matter tracts alone, while synergistic paths are the second-largest contributors (Fig. 3A). This suggests that long-range fibers play a key role in enabling communication between regions that are distant not only physically, but also topologically (the most efficient path between them involves many hops), despite being more metabolically expensive. In addition to this high-level description, however, our approach can also provide more detailed information. We began by considering paths of different length: our framework revealed that synergistic contri-

butions become prevalent for paths comprising multiple hops (Fig. 3B). This may be expected, since the longer the path, the more occasions there may be for making it more efficient with an appropriately-placed connection.

To gain more insight on these results, we repeated our decomposition on networks obtained using a consensus-finding procedure to aggregate individual connectomes [7], which provides two networks that are representative of the topology of long-range and short-range white matter fibers in the human brain (see *Methods*). By decomposing the similarity of these representative pair of networks, we see again that approximately 50% of the maximally efficient paths in the network are accounted for by long-range fibers, confirming the results on individual subjects discussed above (Fig. 4A). Importantly, these analyses allow us to study these networks at the level of individual edges. Results show that that nodes best reached via paths along long-range fibers are predominantly located in different hemispheres, and at opposite ends of the anterior-posterior axis (Fig. 4B). Cross-hemisphere connections are also prominent for synergistic paths. In contrast, redundant and uniquely short-distance paths are primarily located within the same hemisphere (Fig. 4B). This is to be expected, since connecting physically distant nodes by traversing short-

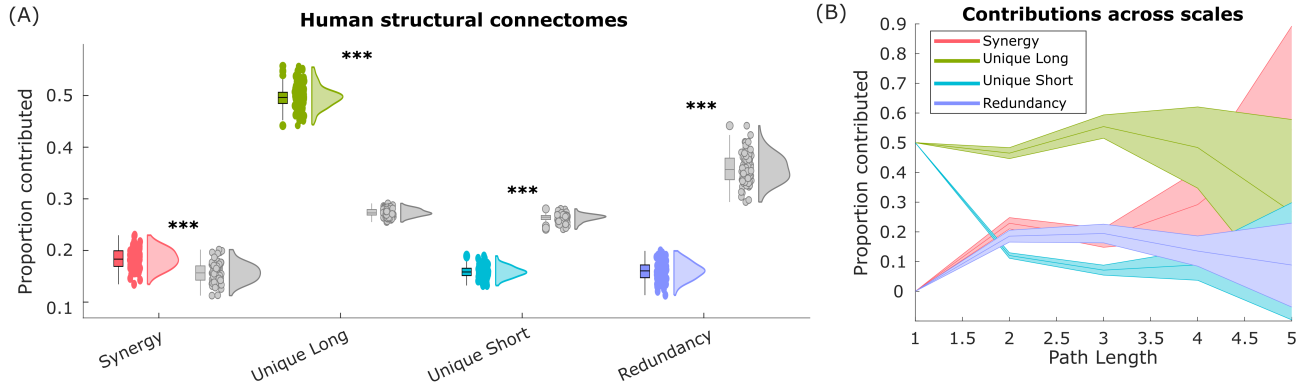


Figure 3. **Prevalence of synergistic, unique, and redundant contributions, for human long- vs short-range structural brain networks.** (A) Proportion of shortest paths accounted for by each PND term. Box-plots indicate the median and inter-quartile range of the distribution. Each data-point is one subject ($N=100$). Grey distributions indicate the corresponding values for degree-preserving randomised networks. ***, $p < 0.001$. (B) Prevalence of synergistic, unique, and redundant contributions as a function of path length, for human structural brain networks.

distance fibers inevitably involves many hops, making this a suboptimal strategy in terms of minimising path length.

To demonstrate the robustness of our results, we show that the same pattern, with long-range tracts accounting for the largest proportion of the maximally efficient paths, can be replicated in an independent dataset of human diffusion MRI, which used Diffusion Spectrum Imaging (Fig. S1) and defined brain regions in anatomical rather than functional terms, including subcortical structures. Likewise, we replicate the human results with a higher-resolution functional parcellation of the cerebral cortex (1000 nodes); in this case, we see an even stronger contribution of synergy (though still second to the unique contribution of long-range tracts), in accordance with the observation that synergy is more prominent with sparser networks (Fig. S1).

We then investigated the role of network topologies in shaping their respective contributions. For this, we consider null models obtained by degree-preserving randomisation of the original structural connectomes. If the networks are randomly rewired (while still preserving the degree sequence), we see that synergy becomes the lowest contributor, and redundancy is the highest (Fig. 3A, grey plots). This is clearly distinct from the predominance of long-range connections observed in the empirical structural connectomes. Statistical comparisons confirm that the human connectome relies on long-range white matter tracts, and synergy between long- and short-range tracts, significantly more than a random network would. On the other hand, the human connectome makes significantly less use of short-range and especially redundant communication pathways (Table S1).

Examining rewired networks enabled us to assess whether the results for the human structural connectomes could be observed just by chance for any network with the same density and degree distribution. Next, we

consider empirical brain networks obtained from a different neuroimaging modality: correlation of functional MRI BOLD signals (i.e., 'functional' connectomes). This enables to ask the question whether any empirical brain networks will display the same pattern of results, or whether those results are specific to the *structural* connectome.

Again, we consider short-range and long-range functional connections as two separate networks, for each individual. What we find is that for functional connections, synergy is by far the main contributor (Fig. 5) — although exhibiting high variability across subjects. Notably, these results related to functional networks greatly differed from the findings related to structural connectivity (both original and randomly rewired). Thus long-range connections play a prominent role in both functional and structural brain networks; but whereas in structural connectomes they play this role mostly in terms of unique contribution, in functional connectomes they do as part of a synergistic contribution.

Structural brain networks across mammalian species

To evaluate if the obtained results are distinctive of the human structural connectome or if this is also observed in other species, we performed analogous analyses over a wide spectrum of structural connectomes from diffusion MRI, covering $N = 220$ individual animals from 125 mammalian species [8, 9] (see *Methods*).

We performed the same analysis as for the human structural connectomes, dividing connections into long-range and short-range ones based on the Euclidean distance between regions, and then identifying the synergistic, redundant, and unique contributions. Similarly to the human structural connectome (and unlike the human functional connectome), our results show that a substan-

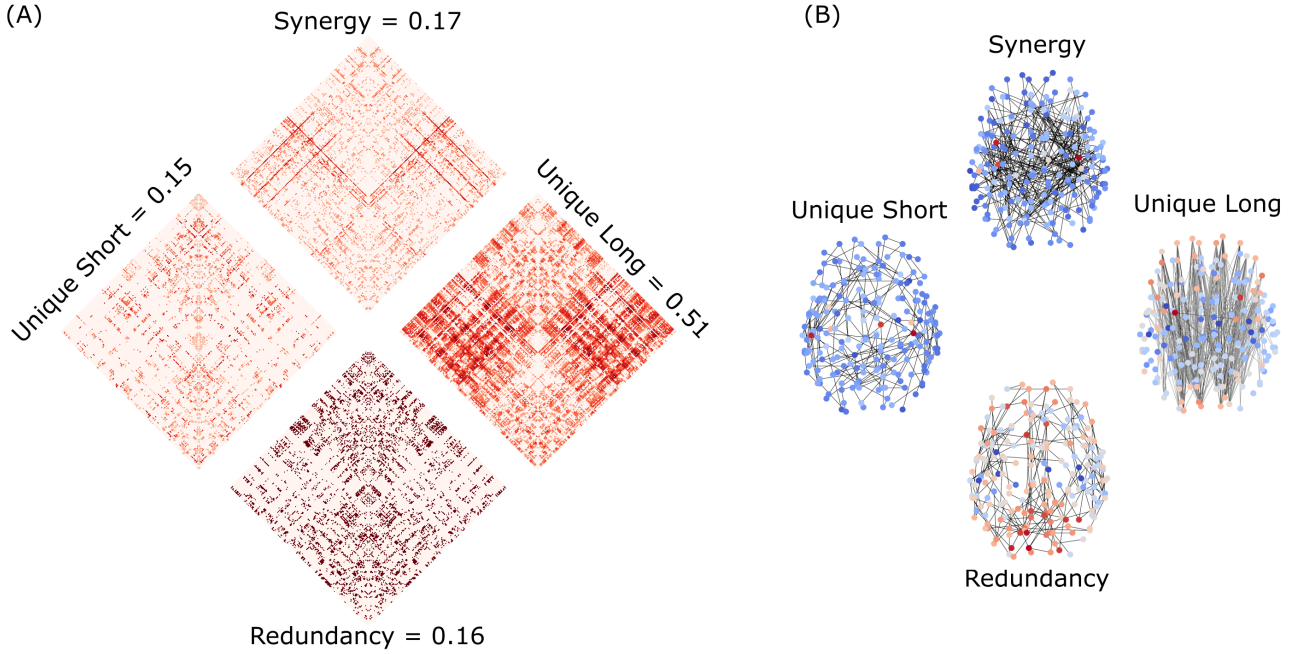


Figure 4. **Edge-wise decomposition into synergistic, unique, and redundant contributions, for group-consensus long- and short-range human structural brain networks.** (A) Each edge is assigned to the network of the corresponding mode, so that each edge is only non-zero in one of the four networks, and its value reflecting the gain in path against the next best alternative. For each matrix, upper and lower quadrants correspond to inter-hemispheric connections, and right and left quadrants are inter-hemispheric. (B) Same as (A), but with edges plotted in the brain to highlight distinct patterns of connectivity in the human brain. Warmer colour indicates higher node degree. Networks are thresholded for visualisation purposes.

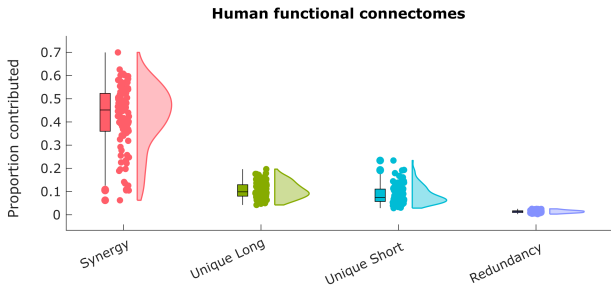


Figure 5. **Prevalence of synergistic, unique, and redundant contributions, for human long- vs short-range functional brain networks** Y-axis: proportion of shortest paths accounted for by each PND term. Box-plots indicate the median and inter-quartile range of the distribution. Each data-point is one subject ($N=100$).

tial proportion of the most efficient paths in the network to be accounted for by long-distance white matter tracts (Fig. 6). Results also show that mammalian structural connectomes are significantly more synergistic and more reliant on long-distance white matter tracts than randomised nulls (see Fig. 6 and Table S2). Unlike the human case, however, we find that non-human mammals also involve a substantial contribution of redundancy be-

tween long-distance and short-distance tracts — though still significantly less than randomly rewired nulls.

Discussion

Here, inspired by the field of information decomposition, we introduced a simple but powerful framework to contextualise two networks with respect to each other. We decompose the most efficient (shortest) paths between nodes as being contributed uniquely by one or the other source networks, or redundantly by either, or synergistically by the two together.

By considering shortest paths, this approach takes into account the topology of the entire networks. It can also provide insights at different levels of resolution: from summary statistics (proportion of all shortest paths contributed by each mode); to information about their relative prevalence across paths of different length; to edge-level detail including the number of steps saved with respect to the next-best alternative.

We showed that this approach can be applied in brain networks as well as transport networks, highlighting the different behaviour of structural and functional connections of different physical length, and their relationship. Finally, we observed that reliance on long-distance white

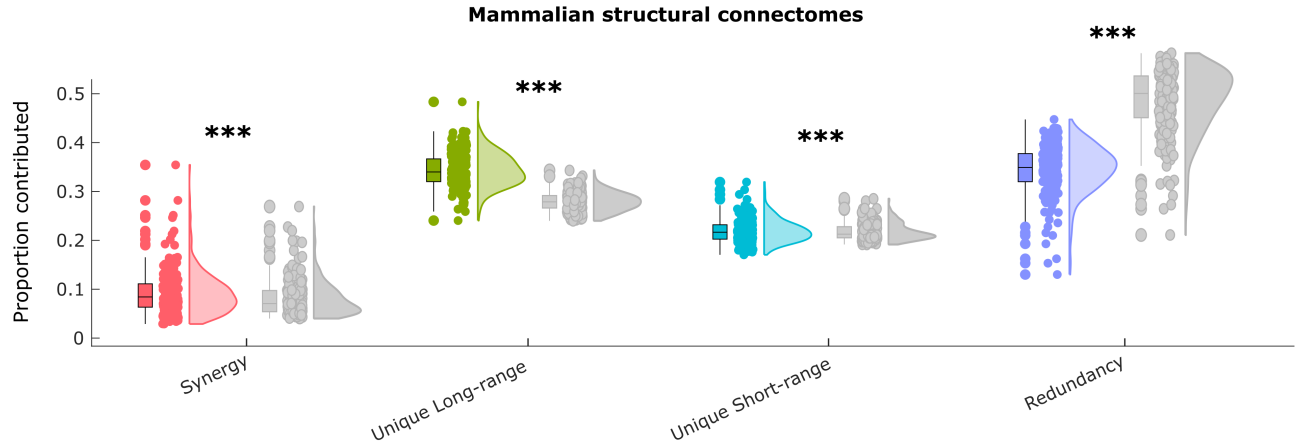


Figure 6. **Prevalence of synergistic, unique, and redundant contributions, for long- vs short-range mammalian structural brain networks.** Grey distributions indicate the corresponding values for degree-preserving randomised networks. Y-axis: proportion of shortest paths accounted for by each PND term. Box-plots indicate the median and inter-quartile range of the distribution. Each data-point is one animal (N=220).

matter fibers for the majority of efficient paths in the network is a conserved feature of mammalian structural connectomes across species. This feature is also observed in humans but differs between human structural and functional networks. We found that the brains of both humans and other mammals also exhibit significantly more synergy, and significantly less redundancy, than corresponding randomly rewired networks. In the London transport networks, redundancy is low in absolute terms, but nevertheless significantly greater than random (though note that the London networks are not predicated in terms of long-range versus short-range connections).

We also found that in general, synergy predominates when both networks are very sparse (approximately 5% density or less) (note that all our comparisons were performed against null models that preserved the original networks’ density and degree, ensuring that such low-level properties do not explain our results). As density in either network grows, synergy rapidly diminishes. This observation is noteworthy because a previous survey suggested that most biological and human-made networks exist in the high-sparsity regime [10] that would be conducive for synergy.

Future directions

Several future extensions of this framework are also possible. First, we only considered when designing network systems, unweighted, undirected networks. A straightforward extension applies to weighted networks, provided that the weights can be combined across the two source networks — as would be the case e.g. for prices or time, in the context of transport networks. Likewise, directed networks can be straightforwardly accommodated.

As with PID, our PID-inspired approach also requires a choice of how to define “path redundancy”. Here, we have adopted equal length of shortest paths as criterion for redundancy. Nevertheless, an interesting alternative is in terms of identity of nodes or edges traversed: will there be a path of length l between nodes x and y even if node z or edge q is taken out? This may contribute to the characterisation of redundancy as robustness.

It is also worth acknowledging that transitioning between networks at a given node is not always possible, and not always free of cost, and this may need to be taken into account for future extensions. As an example: if the cost is time (for transport, for instance), then the time spent while waiting between different transport networks may need to be taken into account; whereas in terms of ticket price, there is often no cost for switching between e.g. different metro lines, but there can be a price for switching between metro and train. This would need to be taken into account when evaluating the advantage conferred by synergy between the two networks.

As a limitation, we note that our use of binary networks required us to threshold the functional connectivity, which imposes a somewhat arbitrary criterion (though not devoid of ground [11]). However, this allowed us to keep the same edge density in the FC and SC networks, thereby removing the influence of density from our results. However, for the London transport example the two networks had different density of edges (Underground vs Overground+DLR); this is going to influence the prevalence of unique paths, since in a binary network an edge corresponds to the shortest (i.e., maximally efficient) possible path between the two nodes at its extremes, so a denser network will have more short paths (whether unique or redundant). Indeed, we found it to be so - but to an extent that was statistically unexpected based on density alone. Future work may extend

the present framework to quantify the extent to which a network uses its available connections synergistically, uniquely, or redundantly, as a proportion of the theoretical maximum for a given partner network.

Here, we used the global efficiency (which is based on shortest paths) as a measure of cost. However, different communication protocols can exist on networks: whereas shortest-path navigation requires knowledge of the global topology, other approaches can be agnostic, such as network diffusion based on random walks, or navigability [12, 13]. Incorporating different communication protocols over networks will be a valuable extension of our framework. One reason that shortest paths are especially appealing for our approach is that, when combining two networks (predicated on the same nodes), the shortest path between nodes x and y can never become longer: only grow shorter (if there is synergy between networks) or remain the same as the shortest of the two. Thus, the path efficiency can only increase or stay the same. However, this property is not guaranteed in the context of diffusion: unless the two networks are identical, the joint network will be denser than either of them, meaning that on average a random walker will have more options to choose between, when leaving node x : although a shortcut to node y may now exist, the average number of steps to reach node y may still increase (because the random walker has more chances of choosing an edge that does not belong to the shortest path – and this repeats at every new node). Therefore, in its present form our framework may often lead to no synergy being identified, when considering communication via random walks.

Relatedly, we note that here we did not consider the question of what dynamics take place over the network [14, 15]. For instance, under dynamics that allow for the possibility of congestion (e.g., traffic), adding a shortcut may not always make travel on the network faster. On the contrary, it may even achieve the opposite effect by increasing congestion — a phenomenon known as “Braess’s paradox” [16]. Thus, two networks that are synergistic in terms of path length may nevertheless end up having “detrimental synergy” in terms of travel time, depending on the dynamics of navigation on the network. It will be a fruitful topic of future investigation to accommodate such scenarios within our framework.

In conclusion, we have developed a simple yet versatile approach to characterise the relationship between two networks, taking into account topological properties and capable of providing both global and local insights. This work may find application when engineering network systems, to help decide how to trade-off different desiderata (such as efficiency vs robustness introduced by a new underground line); or evaluate their relative presence in existing systems, as we have done here for the human brain.

Materials and Methods

Mathematical formalisation

In this section we provide the mathematical foundations of our multiplex network analysis method. It is based on ideas from information theory, which we introduce below, and relies on a mapping between graphs and probability spaces. Beyond the specific metrics showcased in the results of this paper, this formalism paves the way for very general analyses of multiplex networks by combining principles of probability, graphs, and information theory.

Mapping information theory and graphs

A graph can be defined as a pair $(\mathcal{V}, \mathcal{E})$, where \mathcal{V} is a set of vertices (or nodes) and $\mathcal{E} \subseteq \mathcal{V} \times \mathcal{V}$ is a set of edges indexed by pairs of vertices. Our analyses focus on a ‘utility function’ f , which corresponds to a network property of interest. An example of such function is the network’s global efficiency, which is the average of the efficiency between each pair of nodes. For a given node pair $\omega = (v_1, v_2) \in \mathcal{V} \times \mathcal{V}$ in a network with edges \mathcal{E} , we efficiency is defined as the inverse of the length of the shortest path between v_1 and v_2 , and we denote it by $f(\omega; \mathcal{E})$. Additionally, we consider a probability measure $p(\omega)$ uniform over pairs of nodes $\omega \in \mathcal{V} \times \mathcal{V}$, which establishes a random variable Ω . With this, the average value of the utility function f over the network is given by

$$F(\mathcal{E}) = \mathbb{E} [f(\Omega; \mathcal{E})] , \quad (1)$$

where $\mathbb{E} [f(\Omega; \mathcal{E})] = \sum_{\omega} f(\omega) p(\omega)$ is the expected value operator. In the example above, if f is the pairwise efficiency between two nodes, then F corresponds to the global efficiency of the whole network.

Now, suppose that we have two different sets of edges \mathcal{E}_1 and \mathcal{E}_2 for the same set of vertices \mathcal{V} , and we wish to compute how they affect the value of f . For example, a natural question is how much of the value of f can be attributed to the edges in \mathcal{E}_2 , over and above those in \mathcal{E}_1 ? This can be naturally estimated as

$$\Delta F(\mathcal{E}_1 | \mathcal{E}_2) = F(\mathcal{E}_1 \cup \mathcal{E}_2) - F(\mathcal{E}_2) . \quad (2)$$

For example, if F is the global efficiency, then $\Delta F(\mathcal{E}_1 | \mathcal{E}_2) \geq 0$ captures how much the efficiency increases by adding \mathcal{E}_1 to the links in \mathcal{E}_2 .

Using this formalism, a link between graphs and information theory can be established as follows. First, by focusing on the case $f(\omega) = -\log p(\omega)$, then $F(\mathcal{E}_1) = H(\Omega; \mathcal{E}_1)$ corresponds to the entropy of Ω in the network given by $(\mathcal{V}, \mathcal{E})$. In this scenario, ΔF is loosely analogous to a conditional entropy. After establishing how to calculate entropies and conditional entropies over graphs, mutual informations and other quantities can be readily calculated. Therefore, the presented formalism can be seen

as not only linking graphs with standard information-theoretic quantities, but also building a bridge to relate information-theoretic concepts to other utility functions.

Simple example: Decomposing efficiency in two-layer networks

Using the established link between graphs and information theory, one can take inspiration in frameworks to decompose information-theoretic quantities. In particular, here we use ideas from the *Partial Information Decomposition* framework for decomposing the impact of various layers of edges on a given observable. Before presenting the general formalism, here we illustrate the main ideas for a simple case of a two-layered network.

For this, let us consider a multi-layer network \mathcal{M} with vertices \mathcal{V} and two sets of edges (i.e. layers) $\mathcal{E}_1, \mathcal{E}_2$. The full (or joint) network \mathcal{E} contains all edges of both layers, and mathematically is given by the union operator $\mathcal{E} = \mathcal{E}_1 \cup \mathcal{E}_2$. As an example, here we decompose the global efficiency of the joint network $F(\mathcal{E})$ into qualitatively different types of contributions from \mathcal{E}_1 and \mathcal{E}_2 .

Intuitively, for any given pair of vertices v_1, v_2 there are four possibilities: the efficiency could be equal in both layers of the network, it could be greater in one layer than in the other, or it could be greater in the joint network than in either layer. We refer to these different cases as *redundant*, *unique*, and *synergistic*, respectively.

Let us now present a plausible (and empirically powerful) definition for each of these contributions. For a given pair of vertices v_1, v_2 we can take their redundant efficiency (or just *redundancy*) to be the minimum efficiency one could find by using either \mathcal{E}_1 or \mathcal{E}_2 – that is, using the least efficient path fully contained within either of the layers. Mathematically, this can be written as

$$r(v_1, v_2; \mathcal{M}) = \min_i f(v_1, v_2; \mathcal{E}_i) . \quad (3)$$

Based on this formula, the natural definition of the unique contribution of layer \mathcal{E}_j is its gain in efficiency with respect to the redundancy for the same pair:

$$u_j(v_1, v_2; \mathcal{M}) = f(v_1, v_2; \mathcal{E}_j) - r(v_1, v_2; \mathcal{M}) . \quad (4)$$

Note that, with this definition, for any given pair of nodes one layer will have zero unique contribution.

Finally, the synergistic contribution corresponds to the increase in efficiency seen in the joint network but not in either layer. Mathematically:

$$s(v_1, v_2; \mathcal{M}) = f(v_1, v_2; \mathcal{E}) - (r(v_1, v_2; \mathcal{M}) + u_1(v_1, v_2; \mathcal{M}) + u_2(v_1, v_2; \mathcal{M})) . \quad (5)$$

To link back to our explanation above, we can take the expected value of these quantities with respect to $p(\omega)$ (which in the simplest case is an average across all pairs of nodes). This yields the average quantities

$R(\mathcal{M}) = \mathbb{E}[r(\omega; \mathcal{M})]$ and similarly for unique and synergistic contributions. With this, we can write

$$F(\mathcal{E}) = R(\mathcal{M}) + U_1(\mathcal{M}) + U_2(\mathcal{M}) + S(\mathcal{M}) , \quad (6)$$

proving that indeed we have decomposed average global efficiency into four constituent quantities. Note that the global efficiency depends only on the joint network but each atom depends on the full multi-layer network, since they depend on which edges are in \mathcal{E}_1 or \mathcal{E}_2 .

To summarise the overall prevalence of synergistic, unique, and redundant paths in a network, we can define the dominant character of a given node pair $\omega = (v_1, v_2)$ as the highest-order non-zero atom in its partial network decomposition. For example, in the two-layer case described here, we say that ω is a synergistic pair if $s(\omega; \mathcal{M}) > 0$; or a unique pair if $u_j(\omega; \mathcal{M}) > 0$ and $s(\omega; \mathcal{M}) = 0$ (for any j); or a redundant pair if $r(\omega; \mathcal{M}) > 0$ and $s(\omega; \mathcal{M}) = u_j(\omega; \mathcal{M}) = 0$ (for all j).

General framework of Partial Network Decomposition

After presenting an elementary example, let us introduce our full formalism, *Partial Network Decomposition* (PND): an approach to multilayer network analysis inspired by Partial Information Decomposition (PID) [17].

Consider a set of nodes \mathcal{V} and N sets of edges $\{\mathcal{E}_i\}_{i=1}^N$, such that the tuples $(\mathcal{V}, \mathcal{E}_i)$ form networks with the same nodes but different edges. For a given set of indices $a = \{n_1, \dots, n_k\} \subseteq \{1, \dots, N\}$, let's define the joint network $(\mathcal{V}, \mathcal{E}^a)$ with $\mathcal{E}^a = \bigcup_{i=1}^k \mathcal{E}_{n_i}$. Furthermore, let us denote collections of such networks by $\alpha = \{a_1, \dots, a_L\}$. For example, possible collections of networks for $n = 2$ are $\{\emptyset\}, \{\{1\}\}, \{\{1\}, \{1, 2\}\}$, etc.

The key quantity in PND is the *network redundancy function* $F_{\cap}(\mathcal{E}^{a_1}, \mathcal{E}^{a_2}, \dots, \mathcal{E}^{a_L})$, which we will also denote with the shorthand notation F_{\cap}^{α} .

This function should capture how much of the value of F is due to the “common contribution” of all networks $\mathcal{E}^{a_1}, \dots, \mathcal{E}^{a_L}$. We require this function to have the following properties:

Symmetry: $F_{\cap}(\mathcal{E}^{a_1}, \dots, \mathcal{E}^{a_L})$ is invariant to re-ordering of $\mathcal{E}^{a_1}, \dots, \mathcal{E}^{a_L}$.

Self-intersection: $F_{\cap}(\mathcal{E}^a) = F(\mathcal{E}^a)$. This links PND with the original network property of interest, and is analogous to the set-theoretic statement that $S \cap S = S$.

Monotonicity: $F_{\cap}(\mathcal{E}^{a_1}, \dots, \mathcal{E}^{a_k}) \leq F_{\cap}(\mathcal{E}^{a_1}, \dots, \mathcal{E}^{a_{k-1}})$, with equality if $\mathcal{E}^{a_{k-1}} \subseteq \mathcal{E}^{a_k}$. This is analogous to the usual set-theoretic statement that $S \cap T = S$ if $S \subseteq T$.

In principle, one could apply F_{\cap}^{α} to any collection of networks $\alpha \in \mathcal{P}_1(\mathcal{P}_1(\{1, \dots, N\}))$, where $\mathcal{P}_1(S)$ is the power set of S excluding the empty set. However, the monotonicity axiom allows us to simplify the domain of

F_{\cap} : for example, for the two-layer case we know that $F_{\cap}(\mathcal{E}^{\{1\}}, \mathcal{E}^{\{1,2\}}) = F_{\cap}(\mathcal{E}^{\{1\}})$, because $\mathcal{E}^{\{1\}}$ is contained in $\mathcal{E}^{\{1,2\}}$. In the general case, this means we can restrict the domain of F_{\cap}^{α} to the set of *antichains* of $\{1, \dots, N\}$, which are naturally organised in a set-theoretic construct known as a *lattice* [17], denoted here as \mathcal{A} . For the two-layer case, the possible antichains are $\{\{1\}, \{2\}\}$, $\{\{1\}\}$, $\{\{2\}\}$, and $\{\{1, 2\}\}$.

Given a network redundancy function F_{\cap}^{α} , one can also ask how a specific collection of networks α contributes to the overall utility of the joint network. To quantify this, we can define utility “atoms” that capture the contribution of α over and above the contribution of other elements lower in the lattice,

$$F_{\partial}^{\alpha} = F_{\cap}^{\alpha} - \sum_{\beta \prec \alpha} F_{\cap}^{\beta}. \quad (7)$$

This is equivalent to saying that F_{∂}^{α} is the Moebius inversion of F_{\cap}^{α} [17], and can also be written as

$$F_{\cap}^{\alpha} = \sum_{\beta \preceq \alpha} F_{\partial}^{\beta}, \quad (8)$$

which together with the monotonicity property also implies that the sum of all atoms decomposes F as expected,

$$F(\mathcal{E}) = F_{\cap}^{\{\{1, \dots, N\}\}} = \sum_{\alpha \in \mathcal{A}} F_{\partial}^{\alpha}. \quad (9)$$

These atoms are the objects of interest in our analyses, and correspond to the redundant, unique, and synergistic contributions to global efficiency presented in the previous section.

In addition to the formalism above, we need one more ingredient to compute these atoms: a definition of the network redundancy function F_{\cap} . Although more definitions satisfying the properties above could certainly be possible, here we propose the following definition for its suitability and simplicity:

$$F_{\cap}^{\alpha} = \mathbb{E} \left[\min_{a \in \alpha} f(\Omega; \mathcal{E}^a) \right]. \quad (10)$$

With Ω defined as above and f being the efficiency (inverse of the shortest path length), it is easy to see that this definition satisfies the symmetry, self-intersection, and monotonicity axioms above. With this definition, it is possible to evaluate Eq. (10) on all antichains, and then use Eq. (7) to compute all atoms, concluding the calculation. Finally, it is worth noting that, in analogy with the previous section, we can naturally define a redundancy function for node pairs ω , i.e. $f_{\cap}^{\alpha}(\omega) = \min_{a \in \alpha} f(\omega; \mathcal{E}^a)$, such that $F_{\cap}^{\alpha} = \mathbb{E} [f_{\cap}^{\alpha}(\omega)]$ (and similarly for $f_{\partial}^{\alpha}(\omega)$). With this, we can directly generalise our previous definition of the dominant character of a node pair ω as the set α such that $f_{\partial}^{\alpha}(\omega) > 0$ and $f_{\partial}^{\beta}(\omega) = 0 \forall \beta \succ \alpha$.

Data

London transport networks

The network of London public rail transport was obtained from https://networks.skewed.de/net/london_transport. Further details are available from the original publication by De Domenico et al (2014) [18]. It is a multiplex network with 3 undirected edge types representing links within the three layers of London train stations: Underground, Overground and DLR. Here, we combined Overground and DLR into a single network, and we then compared the respective contributions of underground versus overground+DLR (which we refer to as simply “overground”).

Human structural connectomes from Human Connectome Project

We used diffusion MRI (dMRI) data from the 100 unrelated subjects (54 females and 46 males, mean age = 29.1 ± 3.7 years) of the HCP 900 subjects data release [19]. All HCP scanning protocols were approved by the local Institutional Review Board at Washington University in St. Louis. The diffusion weighted imaging (DWI) acquisition protocol is covered in detail elsewhere [20]. The diffusion MRI scan was conducted on a Siemens 3T Skyra scanner using a 2D spin-echo single-shot multiband EPI sequence with a multi-band factor of 3 and monopolar gradient pulse. The spatial resolution was 1.25 mm isotropic. TR=5500 ms, TE=89.50ms. The b-values were 1000, 2000, and 3000 s/mm². The total number of diffusion sampling directions was 90, 90, and 90 for each of the shells in addition to 6 b0 images. We used the version of the data made available in DSI Studio-compatible format at <http://brain.labsolver.org/diffusion-mri-templates/hcp-842-hcp-1021> [21].

We adopted previously reported procedures to reconstruct the human connectome from DWI data. The minimally-preprocessed DWI HCP data [20] were corrected for eddy current and susceptibility artifact. DWI data were then reconstructed using q-space diffeomorphic reconstruction (QSDR [22]), as implemented in DSI Studio (www.dsi-studio.labsolver.org). QSDR is a model-free method that calculates the orientational distribution of the density of diffusing water in a standard space, to conserve the diffusible spins and preserve the continuity of fiber geometry for fiber tracking. QSDR first reconstructs diffusion-weighted images in native space and computes the quantitative anisotropy (QA) in each voxel. These QA values are used to warp the brain to a template QA volume in Montreal Neurological Institute (MNI) space using a nonlinear registration algorithm implemented in the statistical parametric mapping (SPM) software. A diffusion sampling length ratio of 2.5 was used, and the output resolution was 1 mm. A modified FACT algorithm [23] was then used to perform determin-

istic fiber tracking on the reconstructed data, with the following parameters [11]: angular cutoff of 55° , step size of 1.0 mm, minimum length of 10 mm, maximum length of 400 mm, spin density function smoothing of 0.0, and a QA threshold determined by DWI signal in the cerebrospinal fluid. Each of the streamlines generated was automatically screened for its termination location. A white matter mask was created by applying DSI Studio's default anisotropy threshold (0.6 Otsu's threshold) to the spin distribution function's anisotropy values. The mask was used to eliminate streamlines with premature termination in the white matter region. Deterministic fiber tracking was performed until 1,000,000 streamlines were reconstructed for each individual.

For each individual, their structural connectome was reconstructed by drawing an edge between each pair of regions i and j from the Schaefer-200 cortical atlas [24] if there were white matter tracts connecting the corresponding brain regions end-to-end; edge weights were quantified as the number of streamlines connecting each pair of regions.

A consensus matrix A across subjects (consensus connectome) was then obtained using the procedure of Wang and colleagues [25], as follows: for each pair of regions i and j , if more than half of subjects had non-zero connection between i and j , A_{ij} was set to the average across all subjects with non-zero connections between i and j . Otherwise, A_{ij} was set to zero.

Alternative structural connectome from Lausanne dataset

A total of $N = 70$ healthy participants (25 females, age 28.8 ± 8.9 years old) were scanned at the Lausanne University Hospital in a 3-Tesla MRI Scanner (Trio, Siemens Medical, Germany) using a 32-channel head coil [26]. Informed written consent was obtained for all participants in accordance with institutional guidelines and the protocol was approved by the Ethics Committee of Clinical Research of the Faculty of Biology and Medicine, University of Lausanne, Switzerland. The protocol included (1) a magnetization-prepared rapid acquisition gradient echo (MPRAGE) sequence sensitive to white/gray matter contrast (1 mm in-plane resolution, 1.2 mm slice thickness), and (2) a diffusion spectrum imaging (DSI) sequence (128 diffusion-weighted volumes and a single b_0 volume, maximum b -value 8000 s/mm^2 , $2.2 \times 2.2 \times 3.0 \text{ mm}$ voxel size).

Structural connectomes were reconstructed for individual participants using deterministic streamline tractography and divided according to a subdivision of the Desikan-Killiany anatomical parcellation, with 234 cortical and subcortical regions (chosen as the closest match for the 200-node Schaefer parcellation). White matter and grey matter were segmented from the MPRAGE volumes using the FreeSurfer version 5.0.0 open-source package, whereas DSI data preprocessing was implemented with tools from the Connectome Mapper open-source software, initiating 32 streamline propagations per dif-

fusion direction for each white matter voxel. Structural connectivity was defined as streamline density between node pairs, i.e., the number of streamlines between two regions normalized by the mean length of the streamlines and the mean surface area of the regions, following previous work with these data [27, 28].

Human functional connectomes

We used resting-state functional MRI (rs-fMRI) data from the same 100 unrelated subjects of the HCP 900 subjects data release [19]. The following sequences were used: structural MRI: 3D MPRAGE T1-weighted, TR = 2,400 ms, TE = 2.14 ms, TI = 1,000 ms, flip angle = 8° , FOV = 224×224 , voxel size = 0.7 mm isotropic. Two sessions of 15-min resting-state fMRI: gradient-echo EPI, TR = 720 ms, TE = 33.1 ms, flip angle = 52° , FOV = 208 by 180, voxel size = 2 mm isotropic. Here, we used functional data from only the first scanning session, in LR direction.

Functional MRI denoising. We used the minimally preprocessed fMRI data from the HCP, which includes bias field correction, functional realignment, motion correction, and spatial normalization to Montreal Neurological Institute (MNI-152) standard space with 2 mm isotropic resampling resolution [20]. We also removed the first 10 volumes, to allow magnetization to reach steady state. Additional denoising steps were performed using the SPM12-based toolbox CONN (<http://www.nitrc.org/projects/conn>), version 17f [29]. To reduce noise due to cardiac and motion artifacts, we applied the anatomical CompCor method of denoising the functional data. The anatomical CompCor method (also implemented within the CONN toolbox) involves regressing out of the functional data the following confounding effects: the first five principal components attributable to each individual's white matter signal, and the first five components attributable to individual cerebrospinal fluid (CSF) signal; and six subject-specific realignment parameters (three translations and three rotations) as well as their first-order temporal derivatives [29]. Linear detrending was also applied, and the subject-specific denoised BOLD signal time series were band-pass filtered to eliminate both low-frequency drift effects and high-frequency noise, thus retaining frequencies between 0.008 and 0.09 Hz.

Functional network reconstruction. Functional connectivity (FC) networks were obtained for each subject by correlating the BOLD timeseries of each pair of regions in the Schaefer atlas. A group-average FC network was then obtained by averaging across all subjects. To ensure equal footing for the structural and functional networks, the functional networks were each thresholded to have the same density as the corresponding structural network, a procedure termed "structural density matching" [11]. The same was also done for the average functional connectome, which was thresholded at the same

density as the consensus structural connectome. Both structural and functional networks were binarised before analysis.

Mammalian connectomes from diffusion MRI

We used data available online (<https://doi.org/10.5281/zenodo.7143143>); below we provide the main information, with further detail available in the original publication [8]. For consistency of reporting, where possible we use the same wording as recent publications using this dataset [8, 9].

Brain samples. The MaMI database includes a total of 220 ex vivo diffusion and T2- and T1-weighted brain scans of 125 different animal species. No animals were deliberately euthanized for this study. All brains were collected based on incidental death of animals in zoos in Israel or natural death collected abroad, and with the permission of the national park authority (approval no. 2012/38645) or its equivalent in the relevant countries. All scans were performed on excised and fixated tissue. Animals' brains were extracted within 24 hr of death and placed in formaldehyde (10 percent) for a fixation period of a few days to a few weeks (depending on the brain size). Approximately 24 hr before the MRI scanning session, the brains were placed in phosphate-buffered saline for rehydration. Given the limited size of the bore, small brains were scanned using a 7-T 30/70 BioSpec Avance Bruker system, whereas larger brains were scanned using a 3-T Siemens Prisma system. To minimize image artefacts caused by magnet susceptibility effects, the brains were immersed in fluorinated oil (Flourinert, 3M) inside a plastic bag during the MRI scanning session.

MRI acquisition A unified MRI protocol was implemented for all species. The protocol included high-resolution anatomical scans (T2- or T1-weighted MRI), which were used as an anatomical reference, and diffusion MR scans. Diffusion MRI data were acquired using high angular resolution diffusion imaging (HARDI), which consists of a series of diffusion-weighted, spin-echo, echo-planar-imaging images covering the whole brain, scanned in either 60 (in the 7-T scanner) or 64 gradient directions (in the 3-T scanner) with an additional three non-diffusion-weighted images (B0). The b value was 1000 mm^2 in all scans. In the 7-T scans, TR was longer than 12,000 ms (depending on the number of slices), with TE of 20 ms. In the 3-T scans, TR was 3500 ms, with a TE of 47 ms.

To linearly scale according to brain size the two-dimensional image pixel resolution (per slice), the size of the matrix remained constant across all species (128×96). Due to differences in brain shape, the number of slices varied between 46 and 68. Likewise, the number of scan repetitions and the acquisition time were different for each species, depending on brain size and desired signal-to-noise ratio (SNR) levels. To keep SNR levels above 20, an acquisition time of 48 hr was used for small brains

(~ 0.15 ml) and 25 min for large brains (> 1000 ml). SNR was defined as the ratio of mean signal strength to the standard deviation of the noise (an area in the non-brain part of the image). Full details are provided in the original publication [8].

Connectome reconstruction The ExploreDTI software was used for diffusion analysis and tractography [30]. The following steps were used to reconstruct fibre tracts. To reduce noise and smooth the data, anisotropic smoothing with a 3-pixel Gaussian kernel was applied. Motion, susceptibility, and eddy current distortions were corrected in the native space of the HARDI acquisition. A spherical harmonic deconvolution approach was used to generate fibre-orientation density functions per pixel, yielding multiple ($n \geq 1$) fibre orientations per voxel. Spherical harmonics of up to fourth order were used [31]. Whole-brain tractography was performed using a constrained spherical deconvolution (CSD) seed point threshold similar for all samples (0.2) and a step length half the pixel size. The end result of the tractography analysis is a list of streamlines starting and ending between pairs of voxels. Recent studies have shown that fibre tracking tends to present a bias where the vast majority of end points reside in the white matter [31]. To avoid this, the CSD tracking implemented here ensures that approximately 90 percent of the end points reside in the cortical and subcortical grey matter.

Network reconstruction Before the reconstruction of the networks, certain fibre tracts were removed from the final list of tracts. These include external projection fibres that pass through the cerebral peduncle, as well as cerebellar connections. Inner-hemispheric projections, such as the thalamic radiation, were included in the analysis. Brains were parcellated into 200 nodes using a k-means clustering algorithm. All the fibre end-point positions were used as input, and cluster assignment was done based on the similarity in connectivity profile between pairs of end points. Therefore, vertices with similar connectivity profile have a higher chance of grouping together. The clustering was performed twice, once for each hemisphere. Nodes were defined as the mass centre of the resulting 200 clusters. Connectivity matrices were generated by indexing the number of streamlines between any two nodes [8]. The resulting connectivity matrices are hence sparse and weighted adjacency matrices. Matrices were binarized by setting connectivity values to 1 if the connection exists and 0 otherwise.

Even though the sizes of the regions differ across species, we opted for a uniform parcellation scheme (i.e. 200 nodes) for several reasons, in keeping with previous work [9]. First, to our knowledge, there is no MRI parcellation for the brains of the majority of the species studied here. Second, how brain regions correspond to one another across species (i.e. homologues) is still not completely understood for many regions and for many species. Third, comparing networks of different sizes introduces numerous analytical biases because most network measures trivially depend on size, making the com-

parison challenging. We therefore opted to implement a uniform parcellation scheme across species, allowing us to translate connectomes into a common reference feature space in which they can be compared. Note that this approach does not take into account species-specific regional delineations, nor does it capture homologies between nodes across species, which are still not completely understood.

1. Identification of long- and short-range connections

For both human structural and functional networks, as well as mammalian structural networks, connection length was defined in terms of Euclidean distance between the centroids of the regions-of-interest constituting the endpoints of each edge.

A short-range (resp., long-range) connectivity network was obtained as the shortest (resp., longest) 50% of edges. Thus, for each starting network, we obtain a network of its 50% shortest edges, and a network of its 50% longest edges. This approach ensures that both networks have equal density and are therefore on equal terms in terms of their expected contribution to the composite network.

Network null models

To disambiguate the role of connectome topology in shaping the contribution to shortest paths, we relied on network null models [32]. Specifically, we adopted the well-known Maslov-Sneppen degree-preserving rewired network, whereby edges are swapped so as to randomise the topology while preserving the exact binary degree of each node (degree sequence) [33].

Acknowledgments

This research was supported by the Visitor Program of the Max Planck Institute for Mathematics in the Sciences, Leipzig (Germany) [to AIL]. JJ also acknowledges support from Grant 1514 of the German Israeli Foundation.

Conflicts of interest

None.

-
- [1] P. Wills and F. G. Meyer, Plos one **15**, e0228728 (2020).
 - [2] J. P. Bagrow and E. M. Bollt, Applied Network Science **4**, 1 (2019).
 - [3] M. Tantardini, F. Ieva, L. Tajoli, and C. Piccardi, Scientific reports **9**, 1 (2019).
 - [4] L. Lacasa, S. Stramaglia, and D. Marinazzo, Communications Physics **4**, 136 (2021).
 - [5] C. Di Lanzo, L. Marzetti, F. Zappasodi, F. De Vico Fallani, and V. Pizzella, Computational and mathematical methods in medicine **2012** (2012).
 - [6] L. E. Suárez, R. D. Markello, R. F. Betzel, and B. Misic, Trends in Cognitive Sciences **24**, 302 (2020), pMID: 32160567 publisher: Elsevier Ltd.
 - [7] R. F. Betzel, A. Griffa, P. Hagmann, and B. Mišić, Network Neuroscience **3**, 475 (2019), pMID: 30984903 PMID: PMC6444521.
 - [8] Y. Assaf, A. Bouznach, O. Zomet, A. Marom, and Y. Yovel, Nature Neuroscience **23**, 805 (2020).
 - [9] L. E. Suarez, Y. Yovel, M. P. van den Heuvel, O. Sporns, Y. Assaf, G. Lajoie, and B. Misic, Elife **11**, e78635 (2022).
 - [10] G. Melancon, in *Proceedings of the 2006 AVI workshop on BEyond time and errors: novel evaluation methods for information visualization* (2006) pp. 1–7.
 - [11] A. I. Luppi and E. A. Stamatakis, Network Neuroscience **5**, 96 (2021).
 - [12] C. Seguin, M. P. Van Den Heuvel, and A. Zalesky, Proceedings of the National Academy of Sciences **115**, 6297 (2018).
 - [13] C. Seguin, A. Razi, and A. Zalesky, Nature communications **10**, 4289 (2019).
 - [14] U. Harush and B. Barzel, Nature communications **8**, 2181 (2017).
 - [15] C. Kirst, M. Timme, and D. Battaglia, Nature communications **7**, 11061 (2016).
 - [16] D. Braess, Unternehmensforschung **12**, 258 (1968).
 - [17] P. L. Williams and R. D. Beer, arXiv:1004.2515 (2010).
 - [18] M. De Domenico, A. Solé-Ribalta, S. Gómez, and A. Arenas, Proceedings of the National Academy of Sciences **111**, 8351 (2014).
 - [19] D. C. Van Essen, S. M. Smith, D. M. Barch, T. E. Behrens, E. Yacoub, and K. Ugurbil, NeuroImage **80**, 62 (2013), pMID: 23684880.
 - [20] M. F. Glasser, S. N. Sotiropoulos, A. Wilson, T. S. Coalson, B. Fischl, J. L. Andersson, J. Xu, S. Jbabdi, M. Webster, J. R. Polimeni, D. C. Van Essen, and M. Jenkinson, Neuroimage **80**, 105 (2013).
 - [21] F.-C. Yeh, S. Panesar, D. Fernandes, A. Meola, M. Yoshino, J. C. Fernandez-Miranda, J. M. Vettel, and T. Verstynen, NeuroImage **178**, 57 (2018), pMID: 29758339.
 - [22] F.-C. Yeh, V. J. Wedeen, and W.-Y. I. Tseng, NeuroImage **55**, 1054 (2011), publisher: Academic Press.
 - [23] F.-C. Yeh, T. D. Verstynen, Y. Wang, J. C. Fernández-Miranda, and W.-Y. Tseng, PLoS ONE **8**, 80713 (2013).
 - [24] A. Schaefer, R. Kong, E. M. Gordon, T. O. Laumann, X.-N. Zuo, A. J. Holmes, S. B. Eickhoff, and B. T. Yeo, Cerebral cortex **28**, 3095 (2018).
 - [25] P. Wang, R. Kong, X. Kong, R. Liégeois, C. Orban, G. Deco, M. P. Van Den Heuvel, and B. T. Yeo, Science Advances **5**, 1 (2019), pMID: 30662942.
 - [26] A. Griffa, Y. Alemán-Gómez, and P. Hagmann, Zenodo (2019).
 - [27] B. Vázquez-Rodríguez, L. E. Suárez, R. D. Markello, G. Shafiei, C. Paquola, P. Hagmann, M. P. Van Den Heuvel, B. C. Bernhardt, R. N. Spreng, and

- B. Masic, Proceedings of the National Academy of Sciences **116**, 21219 (2019).
- [28] P. Hagmann, L. Cammoun, X. Gigandet, R. Meuli, and C. J. Honey, [PLoS Biol](#) **6**, 159 (2008).
- [29] S. Whitfield-Gabrieli and A. Nieto-Castanon, Brain connectivity **2**, 125 (2012).
- [30] A. Leemans, B. Jeurissen, J. Sijbers, and D. K. Jones, in *Proc Intl Soc Mag Reson Med*, Vol. 17 (2009) p. 3537.
- [31] J.-D. Tournier, F. Calamante, D. G. Gadian, and A. Connelly, *Neuroimage* **23**, 1176 (2004).
- [32] F. Váša and B. Mišić, *Nature Reviews Neuroscience* , 1 (2022).
- [33] S. Maslov and K. Sneppen, [Science](#) **296**, 910 (2002), publisher: American Association for the Advancement of Science.

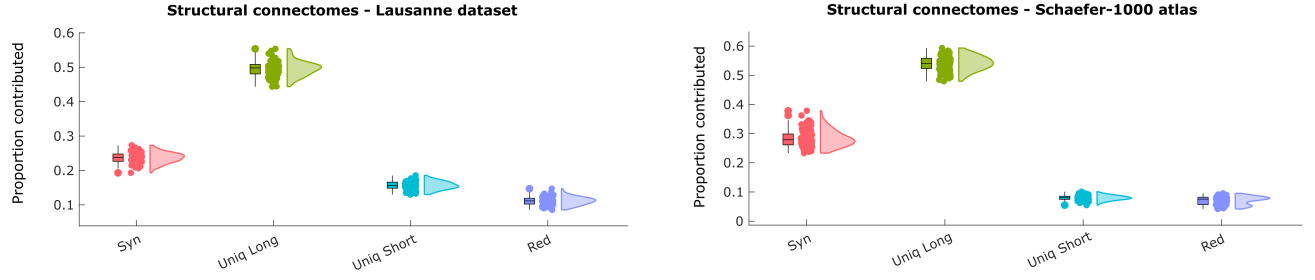


Figure S1. **Replication with alternative reconstruction of the human structural connectome.** Left: connectomes reconstructed from an independent dataset of Diffusion Spectrum Imaging data (N=70 subjects), using the Lausanne anatomical parcellation with 234 cortical and subcortical regions. Right: connectome reconstructed from an alternative sub-parcellation of the Schaefer functional atlas with 1000 cortical nodes (N=100 subjects). Y-axis: proportion of shortest paths accounted for by each PID term. Box-plots indicate the median and inter-quartile range of the distribution. Each data-point is one subject

	Real Mean	Real SD	Null Mean	Null SD	tStat	df	pVal	Hedges g	CI Lower	CI Upper
Synergy	1.84E-01	1.94E-02	1.32E-01	2.05E-02	34.85	99	p < 0.001	2.57	2.31	2.92
Unique Long	4.97E-01	2.15E-02	2.60E-01	8.24E-03	115.65	99	p < 0.001	14.49	12.84	16.93
Unique Short	1.58E-01	1.10E-02	2.51E-01	8.23E-03	-60.48	99	p < 0.001	-9.43	-10.71	-8.46
Redundancy	1.61E-01	1.72E-02	3.57E-01	3.09E-02	-114.75	99	p < 0.001	-7.79	-8.95	-6.99

TABLE S1. Results for the statistical comparison between human structural connectivity networks, and corresponding degree-preserving rewired nulls.

	Real Mean	Real SD	Null Mean	Null SD	tStat	df	pVal	Hedges g	CI Lower	CI Upper
Synergy	9.19E-02	4.46E-02	4.94E-02	4.03E-02	48.01	219	p < 0.001	1	0.85	1.22
Unique Long	3.43E-01	3.38E-02	2.64E-01	1.98E-02	28.15	219	p < 0.001	2.87	2.6	3.19
Unique Short	2.19E-01	2.31E-02	1.98E-01	1.93E-02	13.85	219	p < 0.001	1.02	0.85	1.2
Redundancy	3.45E-01	4.94E-02	4.89E-01	7.12E-02	-50.02	219	p < 0.001	-2.34	-2.73	-2.04

TABLE S2. Results for the statistical comparison between mammalian structural connectivity networks, and corresponding degree-preserving rewired nulls.